Supplementary Information for

# Unravelling high volumetric capacity of $Co_3O_4$ nanograins-interconnected secondary particles for lithium-ion battery anode

Joon Ha Chang,[a,+] Jun Young Cheong,[a,+] Yoonsu Shim,[a,+] Jae Yeol Park,[a] Sung Joo Kim,[a] Jiyoung Lee,[a] Ho Jun Lee,[a] Haeseong Lim,[a] Weiyan Liu,[b] Qing Zhang,[b] Osamu Terasaki,[b] Chan-Woo Lee,[c,*] Il-Doo Kim,[a,*] Jong Min Yuk[a,*]

[a] Department of Materials Science and Engineering, Korea Advanced Institute of Science and Technology, 335 Science Road, Daejeon 34141, Republic of Korea

[b] Center for High-resolution Electron Microscopy (CħEM), School of Physical Science and Technology, ShanghaiTech University, 393 Middle Huaxia Road, Shanghai 201210, China

[c] Platform Technology Laboratory, Korea Institute of Energy Research, 152 Gajeong-Ro, Yuseong-Gu, Daejeon 34129, Republic of Korea

[+] These authors contributed equally to this work.

*e-mail: cwandtj@kier.re.kr, idkim@kaist.ac.kr, jongmin.yuk@kaist.ac.kr

**Bulk, surface and Li adsorbed models calculated by density functional theory (DFT)**

## 1. Bulk models

To further discover why reaction pathway changes under different particle size, density-functional theory (DFT) calculations are performed. Because reaction pathways of both $Co_3O_4$ MPs and $Co_3O_4$ NPs obeserved by *in situ* XRD analyses on Figure 1 contain $LiCo_3O_4$ phase (intercalation phase), we study the conversion reaction after $LiCo_3O_4$ phase depending on different particle size and employed the atomic structure of $LiCo_3O_4$ from the Materials Project, not $Co_3O_4$ spinel structure. According to a previous study [36], octahedral interstial sites of $Co_3O_4$ spinel should be occupied by Co ions when the Li ions inserted and the Li intercalated $Co_3O_4$ structure be tetralgonal rocksalt (Space group: *Cmmm*) that has lattice constant, ***a*** and ***b*** are 8.362 Å and ***c*** is 8.746 Å.

## 2. Surface models

Because this strucuture is composed of $Li^+$ and $Co^{3+}$ layer and $Co^{2+}$ layer which is anisotropic along c-axis, the cleaved surface plane can be 5 types of planes: (001), (100), (110), (101) and (111). We determined the representitive surface model as the most stable (001) plane, Li-O-Co termination and thickness of nine layers converged by surface energy as function of the number of layers (Figure S15). The surface energy, $\gamma$ was calculated by following equation,

$$\gamma = \frac{1}{2A}\left[E_{Li_xCo_yO_z}^{slab} - \frac{N_{Co}}{3}E_{LiCo_3O_4}^{bulk} - \left(N_O - \frac{4}{3}N_{Co}\right)\mu_O - \left(N_{Li} - \frac{1}{3}N_{Co}\right)\mu_{Li}\right]$$

where $E_{Li_xCo_yO_z}^{slab}$ and $E_{LiCo_3O_4}^{bulk}$ are the total energy of slab and bulk; $A$ is the surface area; $N_i$ and $\mu_i$ are the number of atoms and the chemical potential of *i* species respectively. The surface model consists of 36 atoms and 16.895 Å and vacuum was inserted more than 26 Å to avoid

overlap between periodic images. The structures was relaxed by fixing center layer to consider bulk region.We then studied the structural and electrochemical properties of $LiCo_3O_4$ upon the lithiation process after intercalation step, starting from one Li atom adsorped on $LiCo_3O_4$ (001) surface. We empolyed the surface model including 80 atoms which was enlarged from 17.483 $Å^2$ to 69.930 $Å^2$ surface area to avoid too high concentration of adsorbed ion density and removed four layers in bottom to reduce the computational cost.

### 3. Li-adsorbed models

Then we found 8 kinds of Li adsorption sites in the supercell that can be classified by top (T1, T2, T3), bridge (B1, B2) and hollow (H1, H2, H3) sites (Figure S16). The adsorption structures was relaxed by using DFT energy and the adsorption energy was calculated by following equation (Table S2).As a result, Li ion located on bridge sites (B1 and B2) moves to hollow site (H2 and H1) respectively resulting that the bridge site is unstable and Li ion can not stay in there. On the other hands, the adsorption of Li ion on $LiCo_3O_4$ surface is favorable because adsorption energy of top and hollow sites are negative. Especially, the hollow sites are most stable and should be occupied first when Li ion adsorbed.

To describe high concentration of Li ion adsorption, we reduced cell size to 36 atoms allocated in 17.48 $Å^2$ surface area and the adsorbed structure was relaxed by fixing bottom layer to be considered as bulk resulting in lithiated $Co_3O_4$ (001) structure (Fig. 3d)

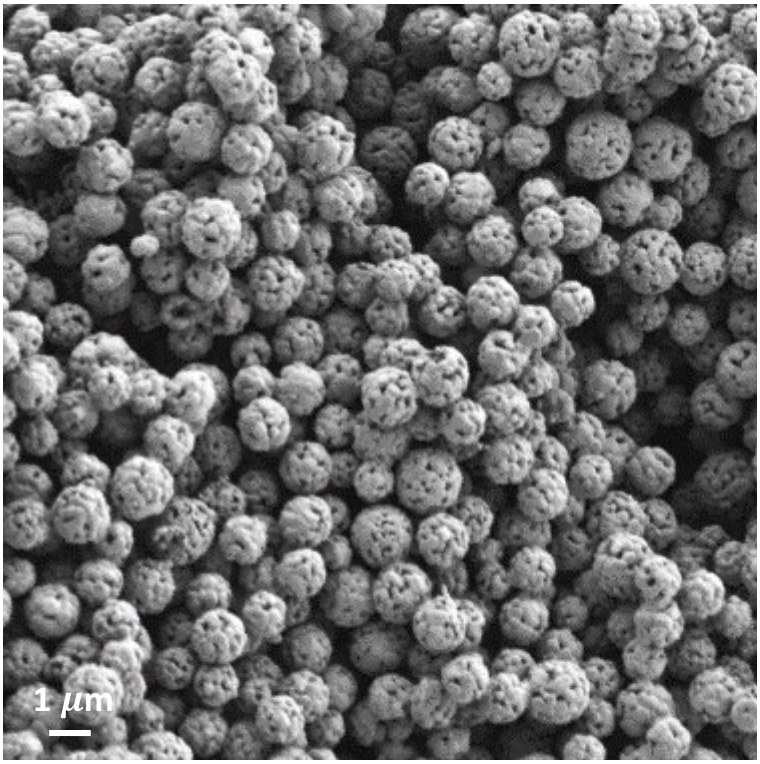


**Fig.S1** Low magnification SEM image of $Co_3O_4$ NISP.

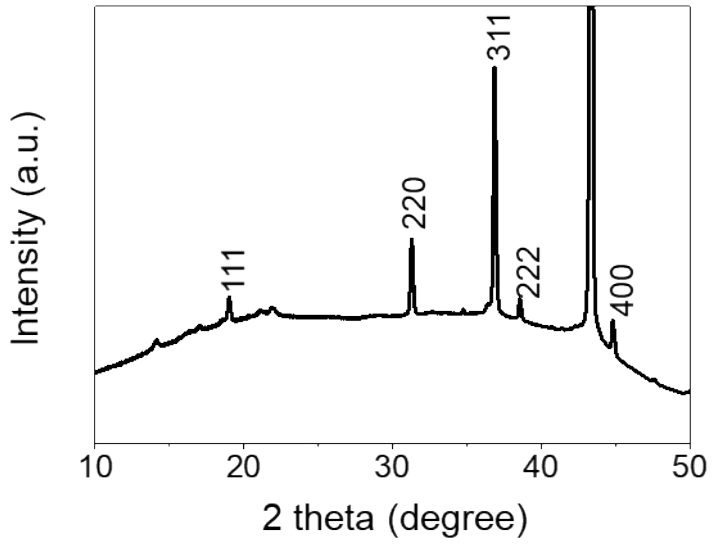


**Fig. S2.** XRD pattern of $Co_3O_4$ NISP, acquired from first pattern of *in situ* XRD experiment. Note that strong peak in 43.3 degree is from Cu foil.

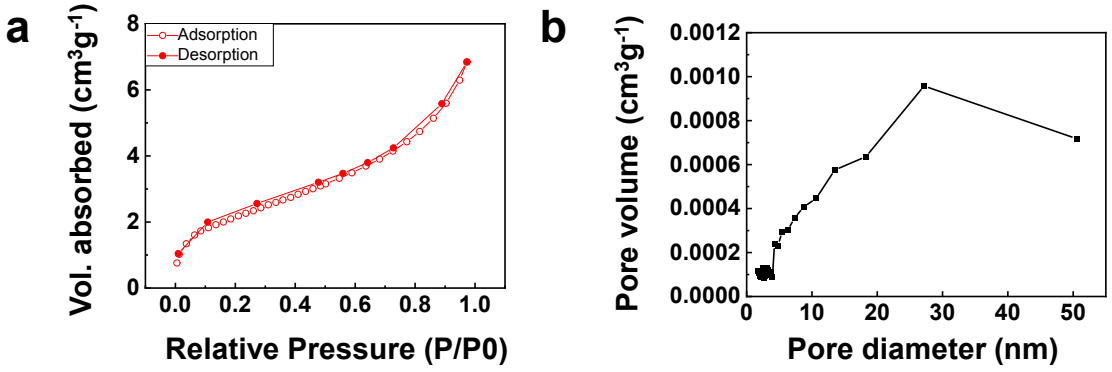


**Fig. S3** (a) Nitrogen adsorption-desorption isotherms and (b) pore size distribution graph of $Co_3O_4$ NISP.

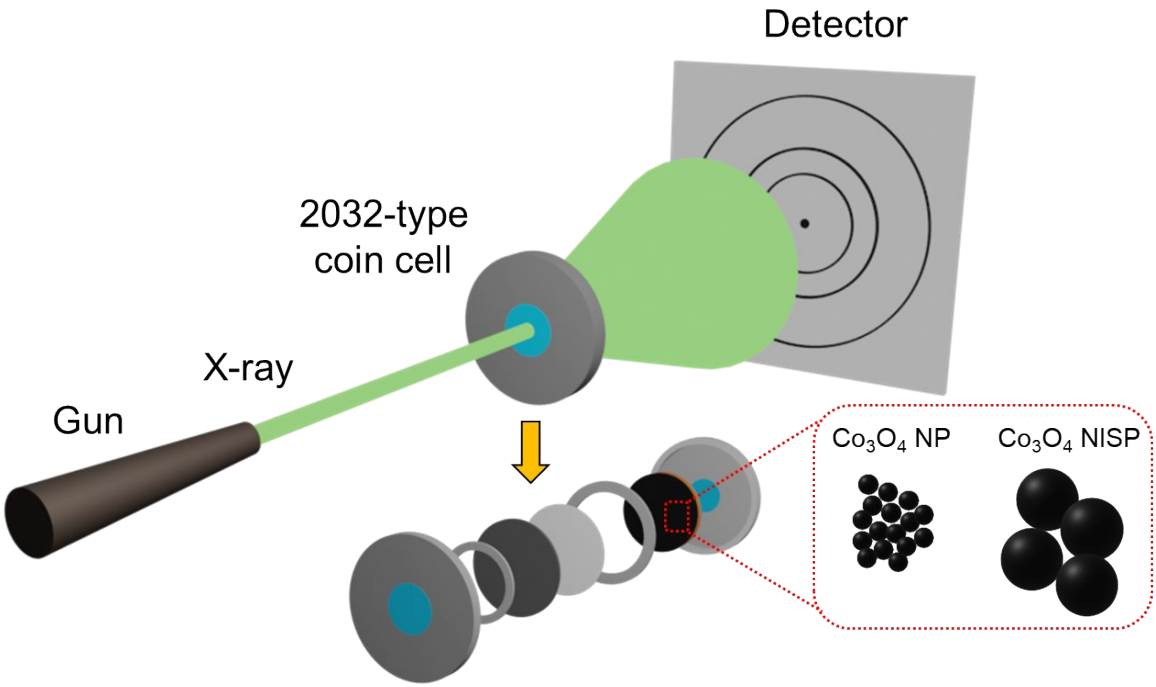


**Fig. S4.** Schematic illustration of *in situ* XRD experiment.

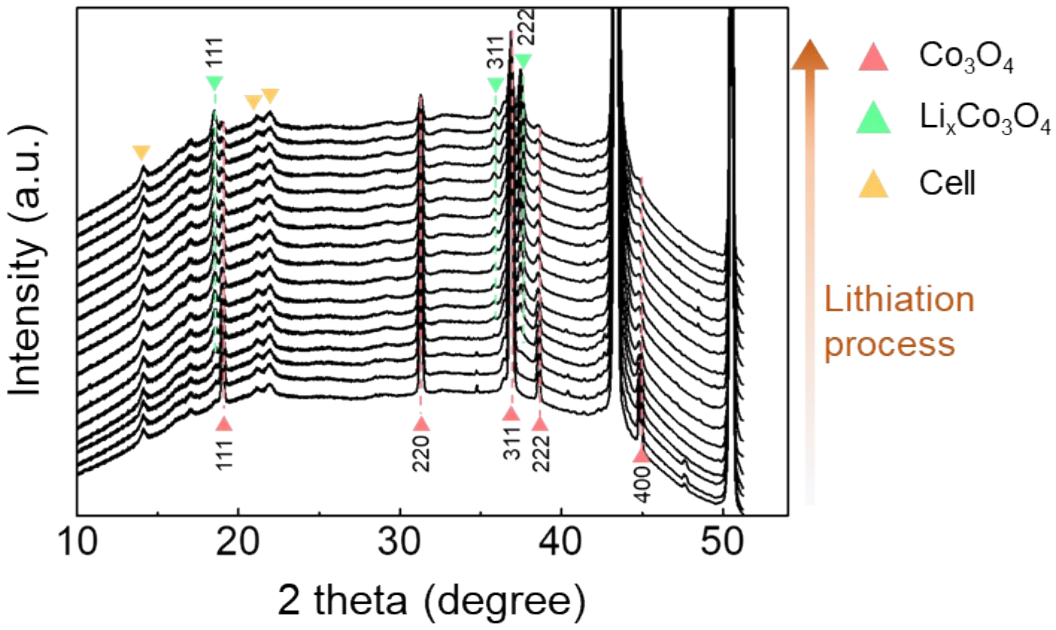


**Fig. S5.** *In situ* XRD patterns $Co_3O_4$ NISP in range of 10 to 55 degree.

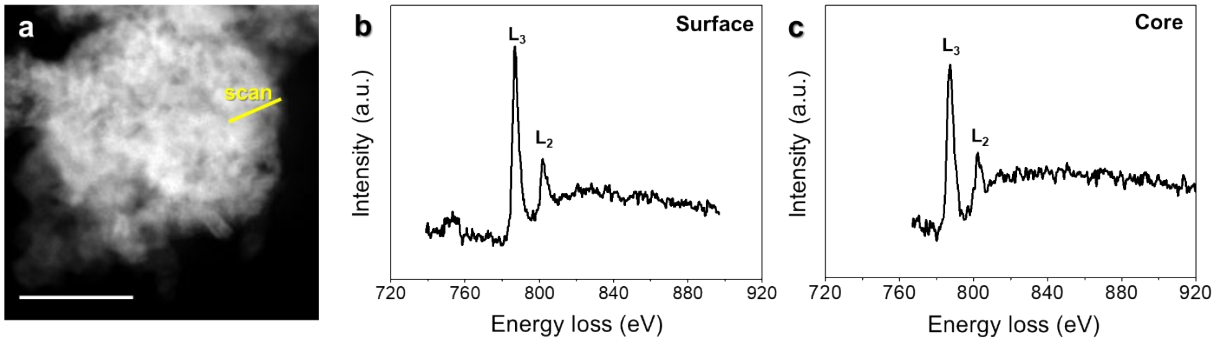


**Fig. S6.** (a) HAADF-STEM image of $Co_3O_4$ NISP at 100% of SOC. (b) EELS spectrum from the surface of $Co_3O_4$ NISP. The ratio between $L_3$ and $L_2$ was 3.36, indicating $Co^{0+}$. (c) EELS spectrum from inner part of $Co_3O_4$ NISP. The ratio was 2.54, indicating 1/3 $Co^{2+}$ and 2/3 $Co^{3+}$. The scale bar in (a) is 500 nm.

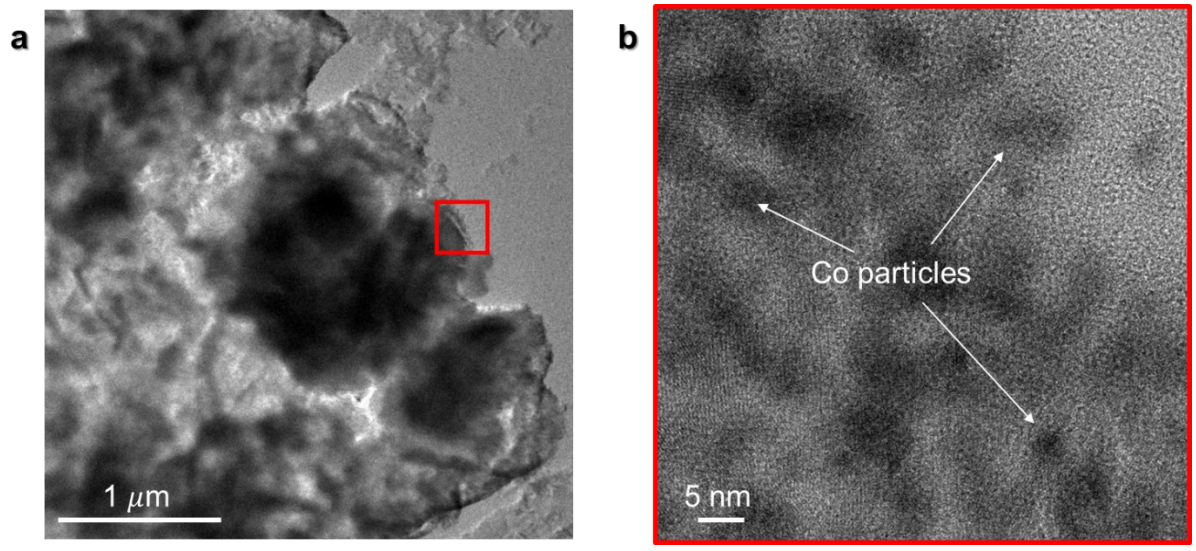


**Fig. S7.** (a) TEM image of $Co_3O_4$ NISP at 100% of SOC. (b) Magnified TEM image of (a), showing Co nanoparticles are present in nanograins.

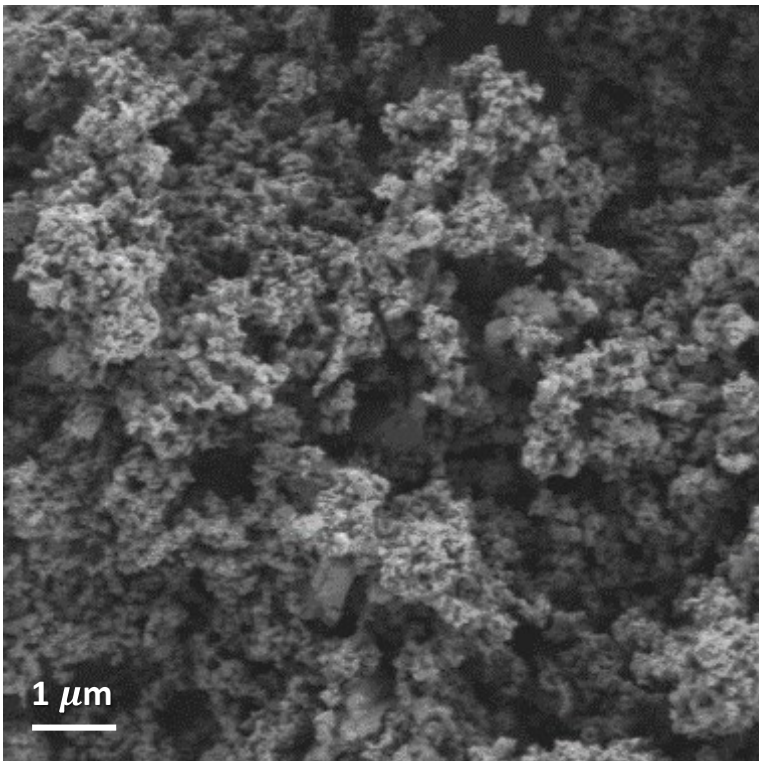


**Fig. S8.** Low magnification SEM image of $Co_3O_4$ NP.

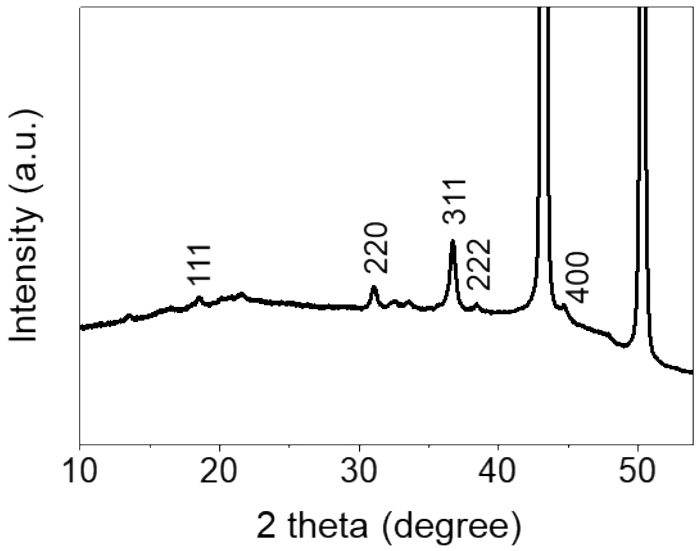


**Fig. S9.** XRD pattern of $Co_3O_4$ NP acquire from first pattern of *in situ* XRD experiment. Note that strong peak in 43.3 and 50.3 degree are from Cu foil.

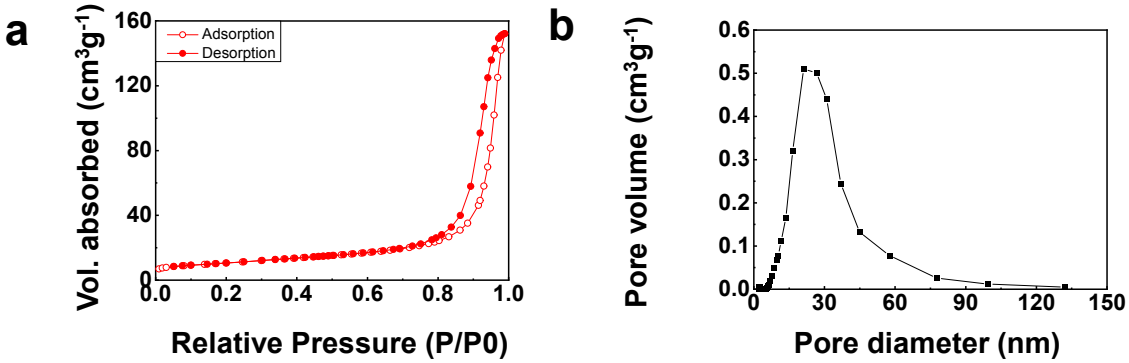


**Fig. S10.** (a) Nitrogen adsorption-desorption isotherms and (b) pore size distribution graph of $Co_3O_4$ NP.

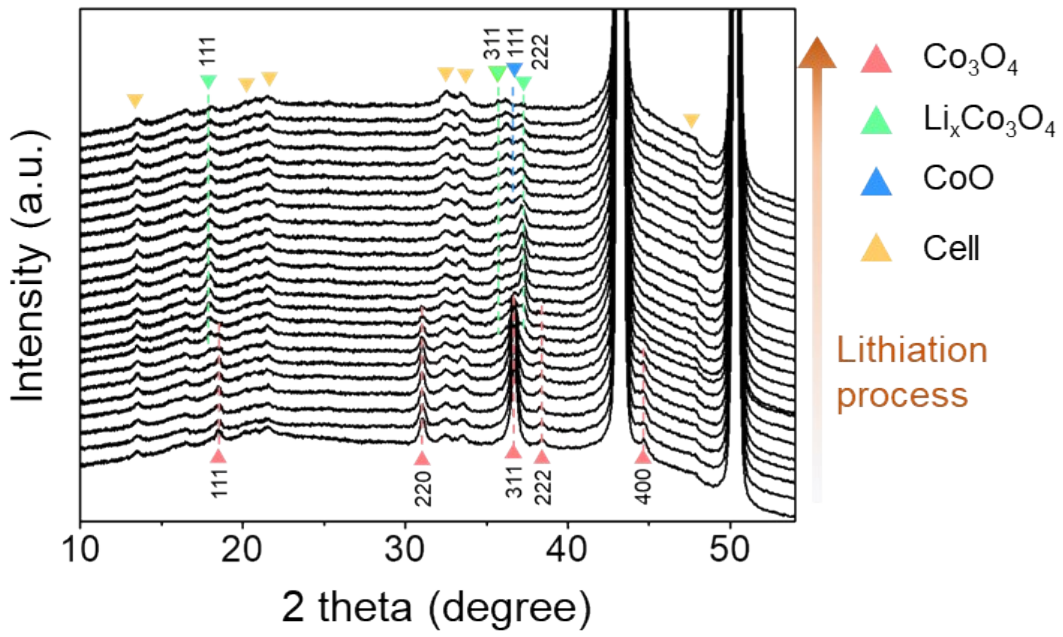


**Fig. S11.** *In situ* XRD patterns $Co_3O_4$ NP in range of 10 to 55 degree.

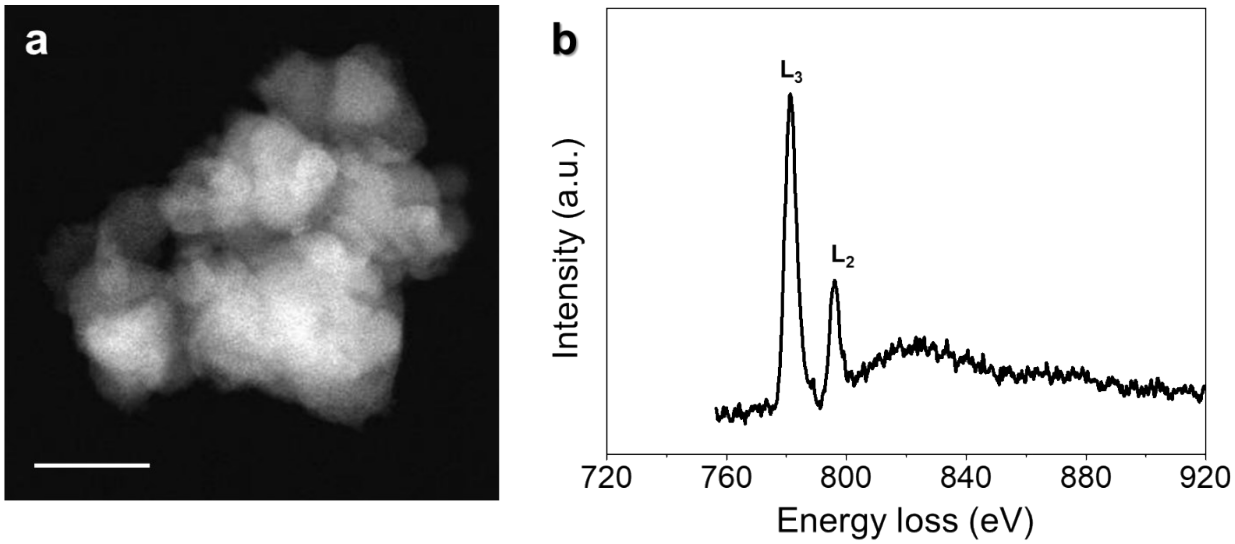


**Fig. S12.** (a) HAADF-STEM image and (b) EELS spectrum of $Co_3O_4$ NP after 1st cycle of lithiation. The ratio between $L_3$ and $L_2$ peak is 3.21, indicating electronic state of $Co^{0+}$. The scale bar in (a) is 100 nm.

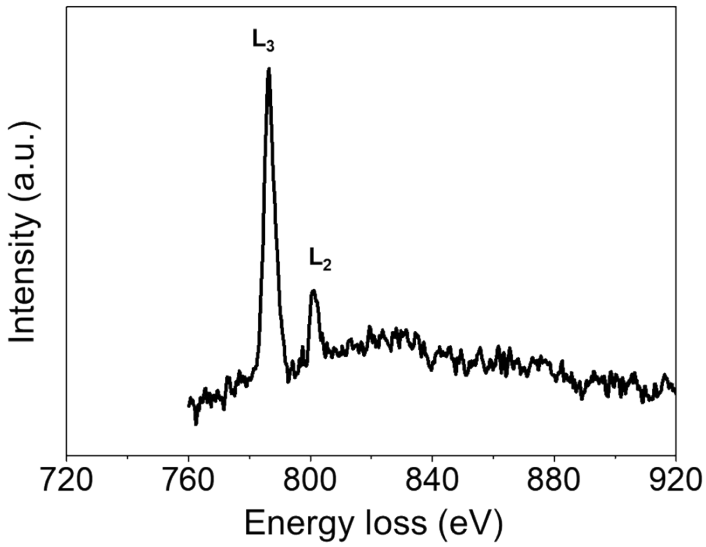


**Fig. S13.** EELS spectrum confirming the presence of CoO on the surface of $Co_3O_4$ NISP, having the peak ratio of 4.55.

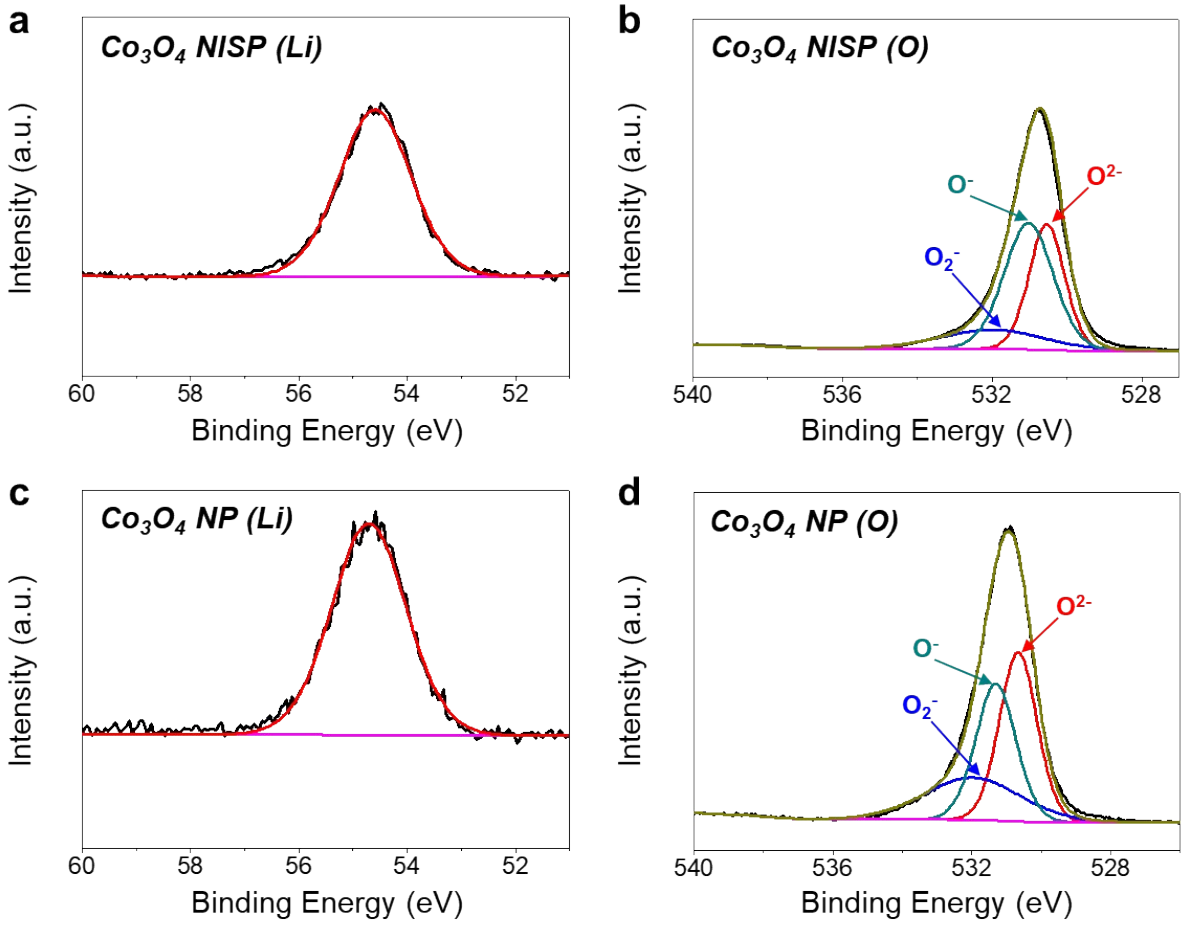


**Fig. S14.** *Ex situ* XPS analysis of (a) Li and (b) O for $Co_3O_4$ NISP after 1st cycle of lithiation. *Ex situ* XPS analysis of (c) Li and (d) O for $Co_3O_4$ NP after 1st cycle of lithiation.

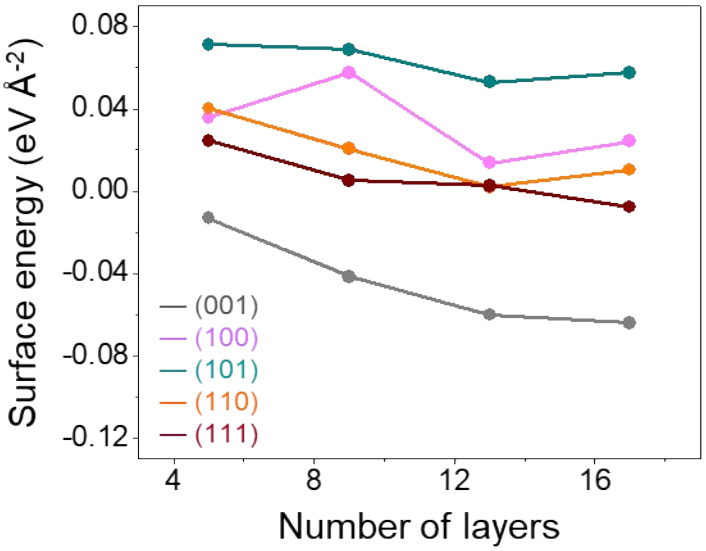


**Fig. S15.** Surface energies of the $LiCo_3O_4$ (001), (100), (101), (110) and (111) surfaces as a function of the number of layers.

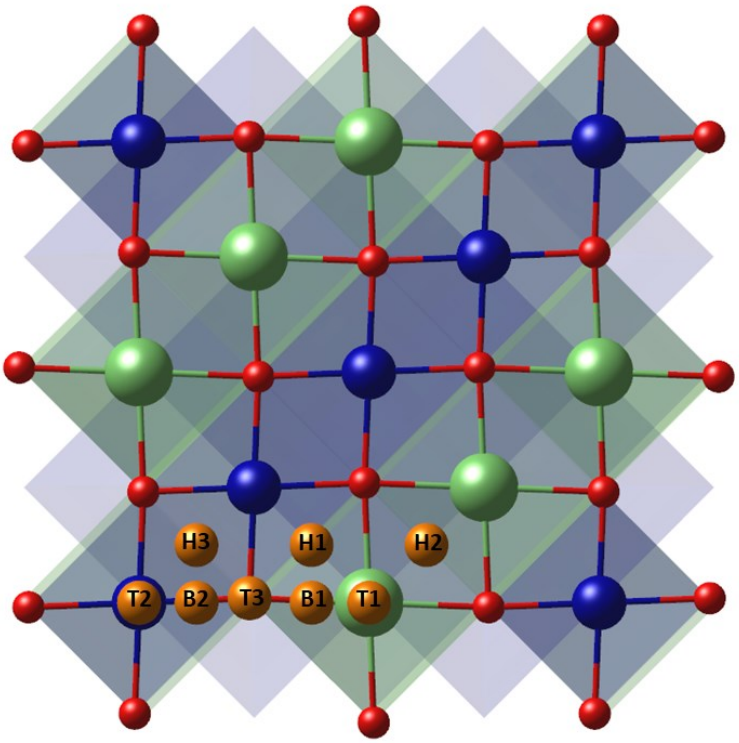


**Fig. S16.** Top view of eight possible Li adsorption sites on the (001) surface: Top sites (T1, T2, T3), bridge sites (B1, B2), and hollow sites (H1, H2, H3).

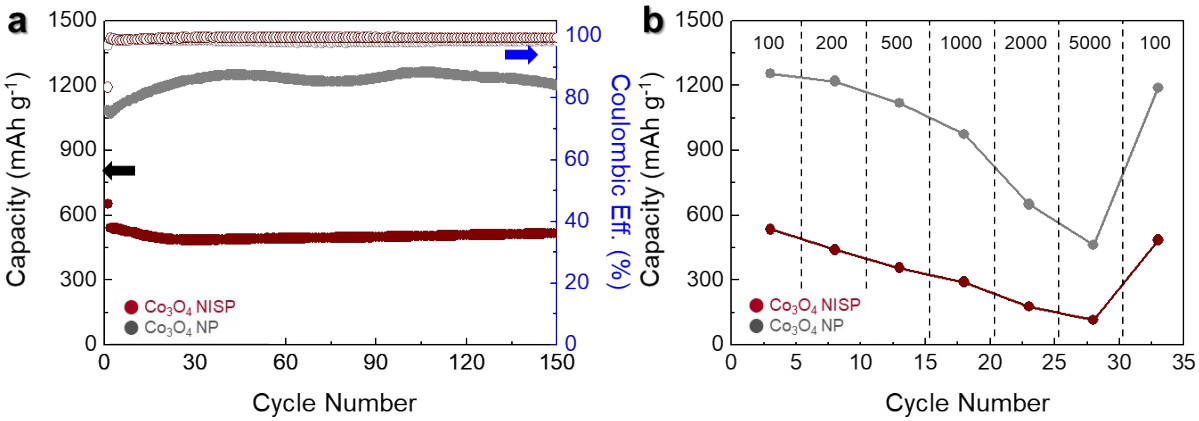


**Fig. S17.** (a) Cycle retention characteristics (at a current density of 500 mA $g^{-1}$) and (b) rate capabilities (at current densities expressed in mA $g^{-1}$) of $Co_3O_4$ NISP and $Co_3O_4$ NP. All units are expressed in terms of gravimetric capacity.

**Table S1.** $L_3/L_2$ ratio of metallic Co and Co oxide [1].

| | $L_3/L_2$ ratio |
|---|---|
| $Co_3O_4$ | 2.42 |
| CoO | 4.51 |
| Metallic Co | 3.15 |

**Table S2.** Adsorption energies with respect to adsorption sites on (001) surface and each site before and after relaxation

| Index | Site (before relaxation) | Site (after relaxation) | $E_{ads}$ (eV) |
|---|---|---|---|
| T1 | Top (Li) | Top (Li) | -0.36 |
| T2 | Top (Co) | Top (Co) | -1.08 |
| T3 | Top (O) | Hollow (Li-O-Li-O) | -1.95 |
| B1 | Bridge (Li-O) | Hollow (Li-O-Li-O) | -2.43 |
| B2 | Bridge (Co-O) | Hollow (Li-O-Co-O) | -1.02 |
| H1 | Hollow (Li-O-Co-O) | Hollow (Li-O-Co-O) | -2.38 |
| H2 | Hollow (Li-O-Li-O) | Hollow (Li-O-Li-O) | -0.29 |
| H3 | Hollow (Co-O-Co-O) | Hollow (Co-O-Co-O) | -1.92 |

**Table S3.** Tap density calculation of $Co_3O_4$ NP and NISP.

| Particle size | Tap density ($g/cm^3$) |
|---|---|
| $Co_3O_4$ NP | 0.5 |
| $Co_3O_4$ NISP | 4.195 |

**Table S4.** Comparison of electrochemical performance and tap density with other previous literatures.

| Spinel type oxides | Tap density (g $cm^{-3}$) | Cycle retention | Rate capabilities | Ref |
|---|---|---|---|---|
| $Li_4Ti_5O_{12}$-C | 1.1 | ~96 mAh $cm^{-3}$ at 7.0 A $g^{-1}$ for 1000 cycles | 103 mAh $cm^{-3}$ at 14.0 A $g^{-1}$ | [2] |
| $Li_4Ti_5O_{12}$ | 1.4 | 235.2 mAh $cm^{-3}$ at 1.0 C For 400 cycles* | 169.4 mAh $cm^{-3}$ at 5.0 C* | [3] |
| $ZnCo_2O_4$ | 1.48 | 1480 mAh $cm^{-3}$ at 0.45 A $g^{-1}$ for 70 cycles* | 1406 mAh $cm^{-3}$ at 0.9 A $g^{-1}$ * | [4] |
| $Fe_3O_4$@CNT | 1.22 | 1540.0 mAh $cm^{-3}$ at 0.1 A $g^{-1}$ for 125 cycles* | 54.9 mAh $cm^{-3}$ at 3.2 A $g^{-1}$ * | [5] |
| $CoMn_2O_4$-S | 1.73 | 1366.7 mAh $cm^{-3}$ at 0.4 A $g^{-1}$ for 100 cycles* | 907.1 mAh $cm^{-3}$ at 1.6 A $g^{-1}$ | [6] |
| $NiFe_2O_4$-S | 1.33 | ~900 mAh $cm^{-3}$ at 0.1 C for 200 cycles | 674.6 mAh $cm^{-3}$ at 2.0 C* | [7] |
| $ZnFe_2O_4$ | 0.85 | 460.7 mAh $cm^{-3}$ at 1.0 A $g^{-1}$ for 488 cycles* | 277.1 mAh $cm^{-3}$ at 1.5 A $g^{-1}$ * | [8] |
| $NiCo_2O_4$-S | 1.66 | 808.4 mAh $cm^{-3}$ at 1.0 C for 1500 cycles | 664 mAh $cm^{-3}$ at 5.0 C | [9] |
| $Co_3O_4$ NISP | 4.195 | 2167.3 mAh $cm^{-3}$ at 0.5 A $g^{-1}$ for 150 cycles | 611.7 mAh $cm^{-3}$ at 5.0 A $g^{-1}$ | This Work |

**References**


[1] Y. Zhao, T.E. Feltes, J.R. Regalbuto, R.J. Meyer, R.F. Klie, *In situ* electron energy loss spectroscopy study of metallic Co and Co oxides, J. Appl. Phys. 108 (2010) 0-7.

[2] Y. Xiang, W. Zhang, B. Chen, Z. Jin, H. Zhang, P. Zhao, G. Cao, Q. Meng, Nano-$Li_4Ti_5O_{12}$ particles in-situ deposited on compact holey-graphene framework for high volumetric power capability of lithium ion battery anode, J. Power Sources 447 (2020) 227372.

[3] J. Ren, H. Ming, Z. Jia, Y. Zhang, J. Ming, Q. Zhou, J. Zheng, High Tap Density $Li_4Ti_5O_{12}$ Microspheres: Synthetic Conditions and Advanced Electrochemical Performance, Energy Technol. 5 (2017) 1680-1686.

[4] R.A. Adams, V.G. Pol, A. Varma, Tailored Solution Combustion Synthesis of High Performance $ZnCo_2O_4$ Anode Materials for Lithium-Ion Batteries, Ind. Eng. Chem. Res. 56 (2017) 7173-7183.

[5] H. Ming, H. Zhou, X. Zhu, S. Zhang, P. Zhao, M. Li, L. Wang, J. Ming, Advanced Metal Oxide@Carbon Nanotube for High-Energy Lithium-Ion Full Batteries, Energy Technol. 6 (2018) 766-772.

[6] S. Chen, Y. Ming, B. Tan, S. Chen, Carbon-free sulfur-based composite cathode for advanced Lithium-Sulfur batteries: A case study of hierarchical structured $CoMn_2O_4$ hollow microspheres as sulfur immobilizer, Electrochim. Acta 329 (2020) 135128.

[7] Z. Zhang, D.-H. Wu, Z. Zhou, G.-R. Li, S. Liu, X.-P. Gao, Sulfur/nickel ferrite composite as cathode with high-volumetric-capacity for lithium-sulfur battery, Sci. China Mater. 62 (2019) 74-86.

[8] L. Hou, H. Hua, L. Lian, H. Cao, S. Zhu, C. Yuan, Green Template-Free Synthesis of Hierarchical Shuttle-Shaped Mesoporous $ZnFe_2O_4$ Microrods with Enhanced Lithium Storage for Advanced Li-Ion Batteries, Chem. Eur. J. 21 (2015) 13012-13019.

[9] Y.-T. Liu, D.-D. Han, L. Wang, G.-R. Li, S. Liu, X.-P. Gao, $NiCo_2O_4$ Nanofibers as Carbon-Free Sulfur Immobilizer to Fabricate Sulfur-Based Composite with High Volumetric Capacity for Lithium-Sulfur Battery, Adv. Energy Mater. 9 (2019) 1803477.